International Journal of Thermal Sciences 49 (2010) 922–930

Contents lists available at ScienceDirect

International Journal of Thermal Sciences

journal homepage: www.elsevier.com/locate/ijts

Visualization study of steam condensation in wide rectangular silicon microchannels

Jiafeng Wu, Mingheng Shi, Yongping Chen*, Xin Li

School of Energy and Environment, Southeast University, Nanjing, Jiangsu 210096, PR China

ARTICLE INFO

Article history:
Received 3 February 2009
Received in revised form
10 January 2010
Accepted 11 January 2010
Available online 11 February 2010

Keywords:
Condensation
Rectangular microchannels
Flow pattern
Heat transfer

ABSTRACT

A visualization study is conducted to investigate condensation flow in wide rectangular silicon microchannels with the hydraulic diameter of 90.6 μm and width/depth ratio of 9.668. Droplet-annular compound flow, injection flow, and vapor slug-bubbly flow are observed along the channel, which differ from that in other cross-sectional shape microchannels. In the droplet-annular compound flow region, the vertical walls (short side) of the channel are completely covered by the condensate, while droplet condensation still exists on the horizontal wall (long side) of the channel. The location of the injection flow will be postponed with the increasing inlet vapor Reynolds number. The injection frequency will increase with the increasing inlet vapor Reynolds number and condensate Weber number. More specifically, the frequency in the wide rectangular microchannels is lower than that in triangular microchannels having the same hydraulic diameter. It is confirmed that the cross-sectional shape of the microchannel plays a significant role on the instability of condensation flow. In addition, the correlation of Nusselt number is also presented.

© 2010 Elsevier Masson SAS. All rights reserved.

1. Introduction

With the development of MEMS thermal devices, such as micro heat pipes, chip laboratories, micro fuel cells and micro thermal control systems, flow condensation in microchannels is turning out to be of considerable importance [1]. Recent experimental results indicate that the physical mechanisms of condensation in microchannels are quite different from those that occur in conventional scale channels. As opposed to the more regular body forces, such as gravity and buoyancy, typically found in common macrochannels, surface tension and shear stress are the dominating forces in microchannels [1–3]. In addition, the cross-sectional shape will deeply influence the flow and heat transfer behavior of condensation in microchannels [4]. However, the understanding of influence mechanisms for channel shape is still insufficient.

The transition of condensation flow patterns is an important subject of the research in microchannels. Garimella et al. [5–8] presented an overview of the visualization study on condensation of refrigerants in minichannels. Their study discussed two-phase flow patterns, heat transfer coefficients and pressure drop of condensation in round, square and rectangular minichannels with hydraulic diameters within the range of 0.5–5 mm. Médéric et al. [3] performed a visualization study of condensation flow patterns in tubes with diameters of 0.56, 1.1 and 10 mm. This observation provided sufficient evidence that the capillary force was dominant in channels with diameters less than 1 mm. Chen et al. [9,10] conducted an investigation of condensation in triangular silicon microchannels with hydraulic diameters less than 250 μm. The results indicated that the channel scale, heat flux, and mass flux all have significant influence on the condensation flow patterns; the droplet flow, annular flow, and injection flow etc. were all observed. Of particular interest here was the new observation of injection flow at a constant frequency, which has received increasing attention in the past several years. Wu et al. [11,12] and Quan et al. [13,14] studied the flow condensation in trapezoidal silicon microchannels; the influence of the condition parameters on the injection flow and the condensation pressure drop in trapezoidal channels were reported. In addition, Zhang et al. [15,16] also investigated the bubble emission and the multichannel effect of condensation in rectangular microchannels. Recently, the flow pattern and heat transfer characteristics of condensation in triangular microchannels were detailed in a study by Chen et al. [17]. The correlations of injection location and frequency with the inlet vapor Reynolds number, condensate Weber number, and hydraulic diameter were acquired based on the experimental data. More specifically, it was found that the condensation heat transfer was enhanced by a reduction in the channel scale. In addition to these experimental investigations, there have been several recent theoretical and numerical studies on condensation in microchannels [18–24].

* Corresponding author. Tel.: +86 25 8379 3092; fax: +86 25 8361 5736.
E-mail address: ypchen@seu.edu.cn (Y. Chen).

1290-0729/$ – see front matter © 2010 Elsevier Masson SAS. All rights reserved.
doi:10.1016/j.ijthermalsci.2010.01.007

Nomenclature

A	heat transfer area of a single channel, m^2
A_c	cross-sectional area of a single channel, m^2
C_c	coefficient of contraction
C_{LM}	Martinelli–Chisholm constant
Co	condensation number
c_p	specific heat of cooling water, J kg^{-1} K^{-1}
D	hydraulic diameter of channel, m
f	exposure frequency of camera, FPS
f_p	injection frequency, Hz
G	volume flow rate of cooling water, m^3 s^{-1}
h_1	enthalpy of condensation flow at inlet, J kg^{-1}
h_2	enthalpy of condensation flow at outlet, J kg^{-1}
L	channel length, m
M	injection periodic number
m_c	mass flow rate of condensation, kg s^{-1}
N	number of photograph
Nu	average Nusselt number of flow condensation
n	channel number
Δp	pressure drop, Pa
q	heat flow rate, W
Re_v	inlet vapor Reynolds number
T_{in}	inlet temperature of cooling water, K
T_{out}	outlet temperature of cooling water, K
$\bar{t}_f$	average temperature of condensation flow, K
t_w	temperature of channel wall, K
$\bar{t}_w$	average temperature of channel wall, K
We_l	condensate Weber number
X	Martinelli parameter
x	shooting position, m
x_p	injection location, m

Greek symbols

α	average heat transfer coefficient of flow condensation, W m^{-2} K^{-1}
α_v	void fraction
β	area ratio of the test section to the header
χ	vapor quality
ϕ_l^2	two-phase friction multiplier
γ	latent heat, J kg^{-1}
υ_v	kinematic viscosity of vapor, m^2 s^{-1}
λ_f	thermal conductivity, W m^{-1} K^{-1}
ρ	density of cooling water, kg m^{-3}
ρ_l	density of condensate, kg m^{-3}
ρ_v	density of vapor, kg m^{-3}
σ	surface tension coefficient, N m^{-1}
ψ_H	homogeneous flow multiplier
ψ_S	separated flow multiplier

However, the understanding of the mechanisms for flow condensation in rectangular microchannels is still insufficient. Due to easy fabrication, rectangular microchannels have been widely used in micro thermal devices, typically using Deep Reactive Ion Etching (DRIE) methods on silicon [25,26]. In addition to being used more often than other shapes, visualization of the flow field in rectangular channels, particularly the wide rectangular microchannels, can be more clearly understood than that in other shapes of microchannels. Therefore, this paper reports an experimental study of flow condensation in wide rectangular silicon microchannels with hydraulic diameter of 90.6 μm, width/depth ratio of 9.668. It is found that the transition of condensation flow patterns in wide rectangular microchannels is different from that occurring in the triangular or trapezoidal microchannels [9–13,17] and rectangular narrows with very large width/depth ratio [15,16]. In addition, both the injection parameters and the heat transfer characteristics of condensation in such rectangular microchannels are presented.

2. Experimental description

2.1. Experimental setup

Ten parallel rectangular microchannels with a width of 483.4 μm and a depth of 50 μm are etched in the silicon wafer using Deep Reactive Ion Etching (DRIE) methods and a Pyrex glass is anodic bonded on the top of the wafer. Fig. 1 is the schematic of the microchannel chip. The hydraulic diameter, D, and width/depth ratio of the channel are 90.6 μm and 9.668, respectively. The effective heat transfer length, L, in each channel is 56.7 mm.

The condensation experiment system shown in Fig. 2 consists of a condensate section, a cooling water cycle system, a data acquisition and a set of high-speed camera device. Saturated steam, which is generated by the boiler, flows successively through the valve, the filter, and then arrives at the wide rectangular silicon microchannels in which the vapor condenses and releases heat to the cooling water in the copper cooler. The silicon chip and the copper cooler are both fixed on an adiabatic workbench and compacted with each other. High-temperature thermally conductive grease is painted on the contact surfaces between the silicon chip and the copper cooler in order to reduce the thermal contact resistance. With the exception of the area for photographing, the whole experimental section is covered by the thermal insulation materials to limit heat loss.

The temperature at the inlet and outlet of condensation flow and cooling water, as well as temperature of the silicon channel wall, are measured by T type thermocouples (accuracy: ±0.1 °C). The inlet and outlet pressure is measured by digital pressure sensor (accuracy: ±1.5 kPa). The volume flow rate of the cooling water is measured by a glass rotor flow meter (accuracy: ±0.4 L/h). Temperature and pressure data is collected by Agilent 34970A data acquisition. The condensation flow pattern is recorded by a microscope having a 2× objective lens and the maximum zoom ratio of 6.4, and a FASTCAM-NET-MAX3 high-speed video camera at the frequency of 125FPS or 250FPS. The injection location, x_p, is measured by a vernier caliper (accuracy: ±0.02 mm). By regulating the pressure of inlet saturated vapor and the temperature and flow rate of cooling water, different experimental conditions can be acquired.

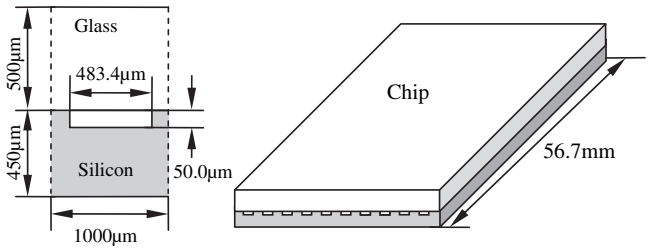

Fig. 1. Schematic of the wide rectangular silicon microchannel chip.

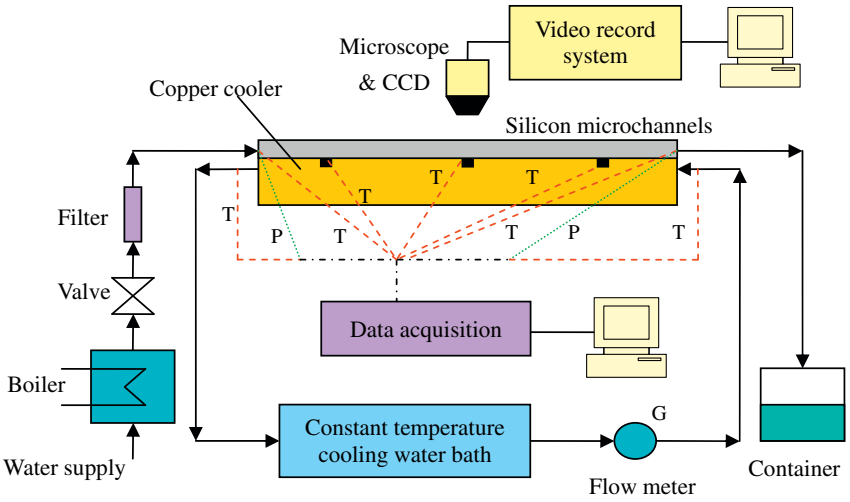

Fig. 2. Schematic of the experimental setup.

2.2. Data reduction

The frequency of the injection flow is acquired from the video recording system. If the exposure frequency of the camera is f, and M injection periodics are recorded by N photographs, the injection frequency f_p can be calculated as

$$f_p = \frac{fM}{N} \tag{1}$$

The average heat transfer coefficient is

$$\alpha = \frac{q}{nA\left(\bar{t}_f - \bar{t}_w\right)} \tag{2}$$

where q is the total heat flow rate of a chip, A is heat transfer area in a single channel, $\bar{t}_w$ is the average temperature of the channel wall, which is the algebraic average of the measured temperatures on the wall surface, $\bar{t}_f$ is the average temperature of the condensation flow, and n is the channel number of the chip, which is 10.

The total heat flow rate is calculated as

$$q = c_p \rho G(T_{out} - T_{in}) \tag{3}$$

where T_{out}, T_{in}, G, c_p and ρ are outlet temperature, inlet temperature, volume flow rate, specific heat and density of the cooling water, respectively. The mass flux of the condensation, m_c, is calculated as

$$m_c = \frac{q}{h_1 - h_2} \tag{4}$$

where h_1 and h_2 are the enthalpy of condensation flow at the inlet and outlet of channel. The inlet saturated vapor enthalpy can be determined by the inlet temperature and pressure, and only the complete condensation flow is considered in this work.

The inlet vapor Reynolds number Re_v and the condensate Weber number We_l are derived by

$$Re_v = \frac{m_c D}{n \upsilon_v \rho_v A_c} \tag{5}$$

$$We_l = \frac{\rho_l D}{\sigma}\left(\frac{m_c}{n\rho_l A_c}\right)^2 \tag{6}$$

where A_c is the cross-sectional area of a single channel, ρ_v and ρ_l are the density of the saturated vapor and condensate, respectively, σ and υ_v are the surface tension coefficient and saturated vapor viscosity, respectively.

The condensation number Co and the average flow condensation Nusselt number Nu in the microchannel are

$$Co = \frac{h_1 - h_2}{\gamma} \tag{7}$$

$$Nu = \frac{\alpha D}{\lambda_f} \tag{8}$$

where γ and λ_f are latent heat and condensate thermal conductivity, respectively.

Considering the whole experimental section is covered by the thermal insulation materials to limit heat loss, except the area for photographing, the heat loss can be assumed to be negligible. Based on the data error analysis, the uncertainties of various parameters in this paper are listed in Table 1.

3. Experimental results

Due to the domination of surface tension and the shear stress, the stratified wavy flow that is a result of gravity in conventional scale channels does not appear in microchannels. This study observed the droplet-annular compound flow, the injection flow, and the vapor slug-bubbly flow, which differed from those in trapezoidal, triangular microchannels [9–13,17] and rectangular narrow channels with very large width/depth ratios [15,16].

3.1. Droplet-annular compound flow

As reported in the literature [9–13,17], droplet condensation takes place near the inlet of the triangular and trapezoidal microchannels. With increasing amount of coagulated droplets on the wall, droplet flow gradually changes to annular flow at the down stream in triangular and trapezoidal microchannels. However, the

Table 1
Uncertainties of parameters.

Parameters	Uncertainties (%)	Parameters	Uncertainties (%)
x_p/L	1.41	Re_v	6.90
f_p	3.15	We_l	9.74
q	6.87	Co	0.32
α	6.92	Nu	6.93

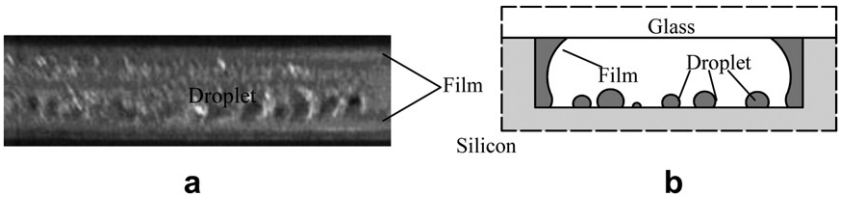

Fig. 3. Droplet-annular compound flow. (a) Experimental photo; (b) Cross-section schematic ($Re_v = 980.3$, $q = 83.1$ W, $x/L = 0.743$).

flow pattern in wide rectangular microchannels is a bit different from that observed in triangular and trapezoidal microchannels. Since the vertical sidewalls are much shorter than the horizontal sidewall and only 50 μm in depth, they will be entirely covered by condensate, in a short distance after the inlet, as shown in Fig. 3. But it is difficult for the condensate to entirely cover the wide horizontal wall to form a conventional annular flow; the droplet flow still exists at the wide horizontal wall, because a hydrophobic fluoropolymer coating is formed on the channel surface during the DRIE etching [27,28]. Thus, a special droplet-annular compound flow is observed in wide rectangular silicon microchannels. At the end of this flow pattern, a periodic alternative injection flow pattern is observed.

3.2. Injection flow

Injection flow is a kind of unstable periodic flow pattern caused by the capillary instability. Since the length of the two-phase zone here is larger than the smallest unstable Rayleigh instability wavelength, both the shear stress and the surface tension have instability influence on the condensation film [29]. Vapor slugs are released periodically at the injection flow region, and this flow pattern is also found in triangular and trapezoidal microchannels [9–13,17] having different vapor slug (or bubble) breakup modes.

Figs. 4 and 5 show the injection flow of condensation in wide rectangular silicon microchannels. Differing from the vapor slug (or bubble) breakup mode in triangular microchannels [17] or in rectangular narrows with very large width/depth ratio [15,16], there are two modes of vapor slug injection flow in rectangular microchannels. The different injection modes indicate the great influence of the cross-sectional shape on the flow condensation in microchannels.

Fig. 4 lists one mode of injection flow including the vapor slug growth and break in wide rectangular microchannels with the inlet vapor Reynolds number, Re_v, of 665.2 and heat flow rate, q, of 58.0 W. This mode is similar to the injection mode in triangular microchannels [17] and one of the injection modes in rectangular narrows [15,16]. The only vapor ligament between the vapor slug and vapor column is very short and periodically variant with the time. As shown in Fig. 4, one vapor slug is emitted within 0.088 s, and the injection frequency, f_p, of this case is about 11.71 Hz. Fig. 5 shows another vapor slug breakup mode with the inlet vapor Reynolds number of 308.9 and heat flow rate of 27.1 W. Differing from that presented in Fig. 4, a long vapor ligament, which is observed neither in the triangular microchannels [17] nor in rectangular narrows [15,16], exists between the vapor slug and vapor column in this mode. In this case, one vapor slug is emitted within 0.232 s and the injection frequency is about 4.231 Hz.

Similar to the flow condensation in the microchannels with other cross-sectional shapes, injection flow is also the characteristic flow pattern in wide rectangular silicon microchannels. Before the injection flow, the channel space is mainly occupied by vapor, the condensate covers the vertical sidewall of the channel and the droplet flow still occurs at the horizontal sidewall, which is in favor of enhancing the condensation heat transfer. However, after the injection, the condensate will occupy the majority of the channel space and the local heat transfer coefficient will be much lower. Recognizing the significance of the injection flow to the condensation heat transfer, it is important to obtain the characteristic parameters of injection flow, such as the location and frequency.

Although injection flow is an unstable flow pattern, the location and the frequency of the injection flow do not alter when the experiment conditions are not changed in the experiments.

In this paper, the injection location is defined as the breakup point of the vapor slug and the vapor column. Fig. 6 shows the variation of dimensionless injection location, x_p/L, versus the inlet vapor Reynolds number, Re_v, in the wide rectangular microchannels. And the experimental results are compared with those in triangular silicon microchannels with sidewalls inclined at 54.7° under the same conditions (with the same hydraulic diameter D and condensate number Co) [17] to show the influence of the channel cross-sectional shape. As shown in Fig. 6, the dimensionless injection location increases with the increasing inlet vapor Reynolds number, which is similar to the experimental results in triangular microchannels. At the same inlet vapor Reynolds number, the dimensionless injection location in wide rectangular microchannels is much larger than that in triangular microchannels.

Based on the experimental data, a correlation of dimensionless injection location and inlet vapor Reynolds number in the wide rectangular microchannel is presented as

$$x_p/L = 1.253 \times 10^{-4} Re_v^{1.324} \quad (9)$$

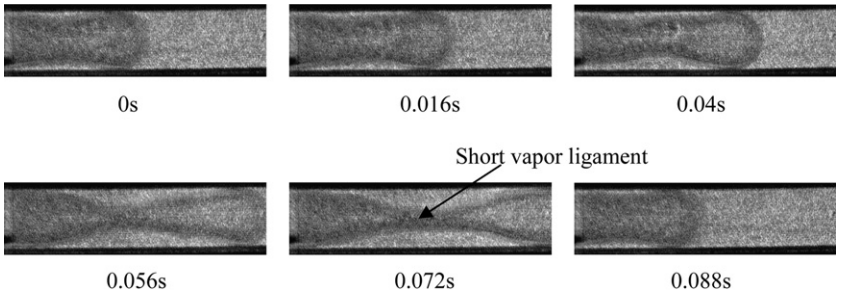

Fig. 4. Injection flow in wide rectangular microchannels (condition 1). ($Re_v = 665.2$, $q = 58.0$ W, $x_p/L = 0.7469$, $f_p = 11.71$ Hz.)

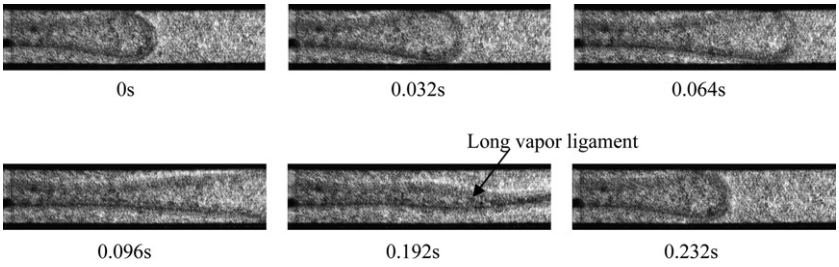

Fig. 5. Injection flow in wide rectangular microchannels (condition 2). ($Re_v = 308.9$, $q = 27.1$ W, $x_p/L = 0.2310$, $f_p = 4.231$ Hz.)

The locations of injection flow predicted by Eq. (9) are compared with the experimental data in Fig. 7 and Table 2. The correlation coefficient and the maximum deviation of Eq. (9) from the experimental data are 0.9851 and 8.98%, respectively.

Figs. 8 and 9 show the relationship of the injection frequency, f_p, versus inlet vapor Reynolds number, Re_v, and condensate Weber number We_l, respectively, compared to those in triangular microchannels [17]. The injection frequency in wide rectangular microchannels increases with the increase of the inlet vapor Reynolds number and the condensate Weber number.

Based on the experimental data, the correlation of injection frequency and inlet vapor Reynolds number in the wide rectangular microchannel is presented as

$$f_p = 9.591 \times 10^{-5} Re_v^{1.834} \quad (10)$$

The locations of injection flow predicted by Eq. (10) are compared with the experimental data in Fig. 10 and Table 2. The correlation coefficient and the maximum deviation of Eq. (10) from the experimental data are 0.9623 and 25.9%, respectively.

Compared with that in triangular microchannels, the injection frequency in rectangular microchannels is much smaller. This experimental result indicates the significant effect of cross-sectional shape on the condensation instability in microchannels. Since the condensate film is turning to be more unstable with the decreasing vapor core diameter in microchannels [29], the influence of the cross-sectional shape on the vapor core hydraulic diameter maybe a chief reason for the influence of the channel cross-sectional shape on the instability. Fig. 11 shows the variation of the vapor hydraulic diameter versus the void fraction, α_v, in the wide rectangular and triangular microchannels having the same channel hydraulic diameter of 90.6 μm. As shown in the figure, the vapor hydraulic diameter in rectangular microchannel is larger than that in the triangular microchannel, when the void fraction is smaller than 0.6. It means that the condensate film at the small void fraction sections in triangular microchannels is more unstable than that in the rectangular microchannels.

In addition, the injection flow can and only can be formed when the liquid bridge are constructed. In other words, the injection only occurs at the small void fraction sections. Therefore, the injection flow is more frequently generated in triangular microchannels.

3.3. Vapor slug-bubbly flow

The vapor in emitted vapor slug and the condensate will be further cooled after the injection flow. The two-phase condensation flow pattern after the injection flow is called the vapor slug-bubbly flow, which is another important flow pattern of condensation. Considering the bubble size, the vapor slug-bubbly flow can be divided into two flow patterns: the vapor slug flow (see Fig. 12) and the bubbly flow (see Fig. 13). The bubble size of the vapor slug flow is larger than that of the bubbly flow, and the vapor slug takes a long column shape in the wide rectangular microchannel with a hemisphere at head, under the control of the surface tension. The vapor slug flow can be generated by either the injection (see Fig. 12) or the vapor slug (or bubble) combination. Although the vapor slug flow pattern is also observed in the condensation process of the triangular and trapezoidal silicon microchannels [9–13,17], there is no report of this flow pattern [15,16] in the rectangular narrows with very large width/depth ratio. The existence of the vapor slug flow is one of the distinctions between the wide rectangular microchannels and the rectangular narrows. As the vapor in the slug condenses, the vapor slug flow will turn into the bubbly flow at the down stream.

As shown in Fig. 13, the remaining vapor is contracted to form a round shape under the control of surface tension in the bubbly flow region. The majority of the channel space is occupied by the

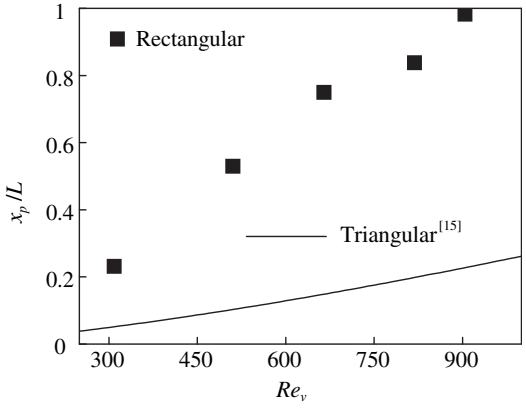

Fig. 6. Injection location versus inlet vapor Reynolds number. ($D = 90.6$ μm, $Co = 1.065$.)

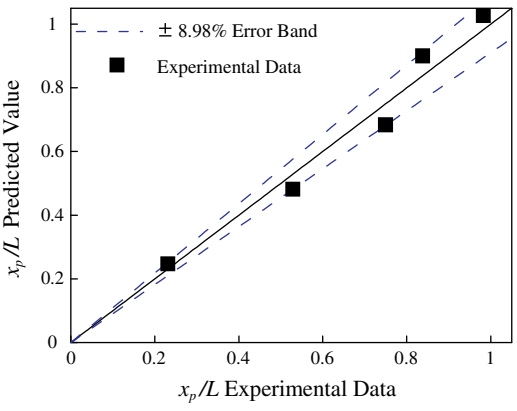

Fig. 7. Comparison between the predicted and experimental values of dimensionless injection location. (The same condition with Fig. 6.)

Table 2
Experimental data points and fitting values (the same condition with Fig. 6).

Re_v	x_p/L			f_p (Hz)			Nu		
	Experimental data	Fitting value	Relative error (%)	Experimental data	Fitting value	Relative error (%)	Experimental data	Fitting value	Relative error (%)
904.2	0.9824	1.027	4.52	32.51	25.30	−22.2	1.299	1.324	1.92
818.6	0.8377	0.9002	7.45	21.21	21.08	−0.578	1.296	1.231	−5.00
665.2	0.7496	0.6839	−8.76	11.71	14.40	23.0	0.9846	1.057	7.40
510.4	0.5291	0.4816	−8.98	7.040	8.864	25.9	0.9157	0.8708	−4.90
308.9	0.2310	0.2477	7.21	4.231	3.529	−16.6	0.5959	0.6026	1.12

condensate. Only a little part of vapor still exists in the bubbles, and these bubbles flow very quickly along the channel. The collision and combination of bubbles may occur in the microchannel and generate a larger bubble. Fig. 13 recorded a combination process of two bubbles within 0.08 s. The spherical bubbles without combination will gradually condense, shrink, and submerge in the condensate.

More specifically, bubbles can be observed at the outlet of the channel in many cases, where the condensate has been sub-cooled. And the outlet condensate temperature is lower than the saturation temperature, which means the condensation has been completed.

3.4. Flow and heat transfer characters

In addition to the visualization study on the condensation flow pattern, this paper also investigates the flow and heat transfer characteristics in wide rectangular microchannels. Figs. 14 and 15 illustrate the variations of wall temperature, t_w, and the total pressure drop of the condensation, Δp, versus the inlet vapor Reynolds number, Re_v, respectively. As shown in the figures, the wall temperature decreases along the flow direction, and the average wall temperature and the total pressure drop will increase with the increasing inlet vapor Reynolds number.

As shown in Fig. 15, the total pressure drop is also predicted by using the conventional correlations developed for condensation inside conventional tubes. It is calculated as [7,8]

$$\Delta p_{\text{predicted}} = \int_0^L \left(\frac{dp_{\text{friction}}}{dx} - \frac{dp_{\text{deceleration}}}{dx} \right) dx + \Delta p_{\text{contraction}} - \Delta p_{\text{expansion}} \quad (11)$$

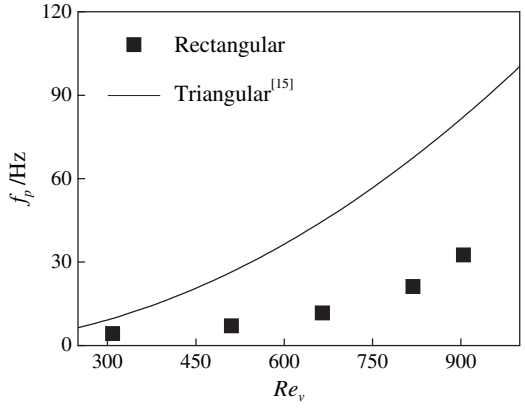

Fig. 8. Injection frequency versus inlet vapor Reynolds number. (The same condition with Fig. 6.)

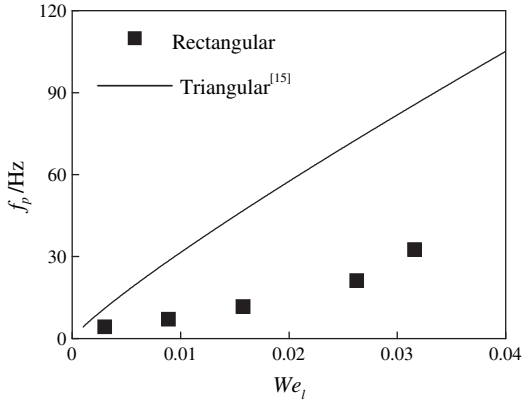

Fig. 9. Injection frequency versus condensate Weber number. (The same condition with Fig. 6.)

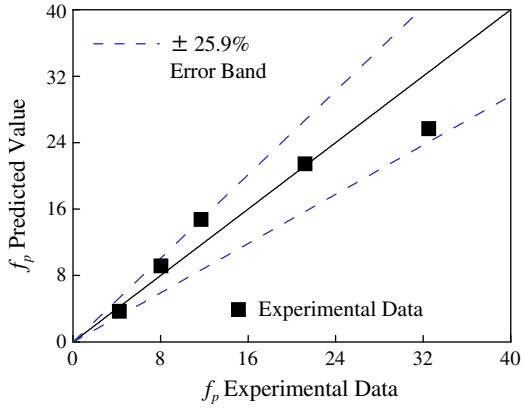

Fig. 10. Comparison between the predicted and experimental values of injection frequency. (The same condition with Fig. 6.)

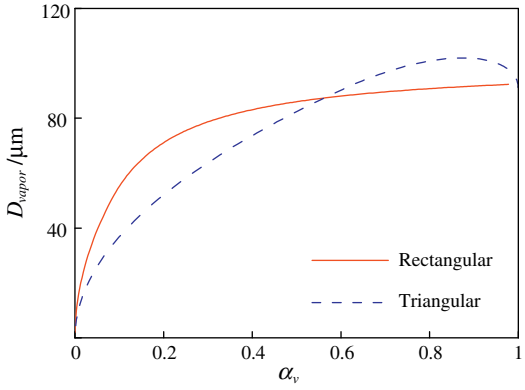

Fig. 11. Hydraulic diameter of vapor core versus the void fraction in rectangular and triangular microchannels. ($D = 90.6$ μm.)

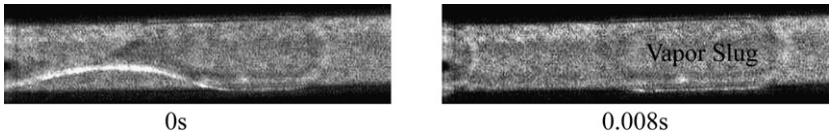

Fig. 12. Vapor slug flow generated by injection. ($Re_v = 818.6$, $q = 72.6$ W, $x_p/L = 0.8377$.)

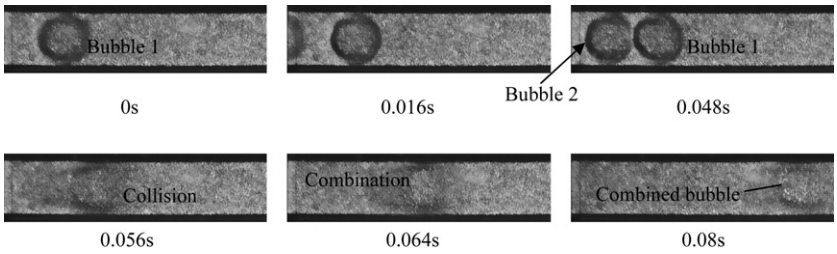

Fig. 13. Bubble combination. ($Re_v = 677.3$, $q = 57.8$ W, $x/L = 0.919$.)

where $dp_{friction}/dx$ is the frictional pressure drop per unit length of the two-phase flow, which can be calculated by the Lockhart–Martinelli correlation [30]

$$\frac{dp_{friction}}{dx} = \phi_l^2 f_l \frac{(1-\chi)^2}{2\rho_l D}\left(\frac{m_c}{nA_c}\right)^2 \tag{12}$$

where f_l is the friction factor of the condensate, χ is the vapor quality, and the two-phase friction multiplier ϕ_l^2 is given by [14]

$$\phi_l^2 = 1 + \frac{C_{LM}}{X} + \frac{1}{X^2} \tag{13}$$

where X is the Martinelli parameter and C_{LM} is the Martinelli–Chisholm constant.

$dp_{deceleration}/dx$ is the deceleration pressure drop per unit length, which is given by

$$\frac{dp_{deceleration}}{dx} = \left| G^2 \frac{d}{dx}\left[\frac{\chi^2}{\rho_l \alpha_v} + \frac{(1-\chi)^2}{\rho_v(1-\alpha_v)}\right]\right| \tag{14}$$

And $\Delta p_{contraction}$ and $\Delta p_{expansion}$ are the contraction pressure at channel inlet and the expansion pressure at the channel outlet, respectively. They are calculated as [7]

$$\Delta p_{contraction} = \frac{1}{2\rho_l}\left[1 - \beta^2 + \left(\frac{1}{C_c} - 1\right)^2\right]\psi_H \left(\frac{m_c}{nA_c}\right)^2 \tag{15}$$

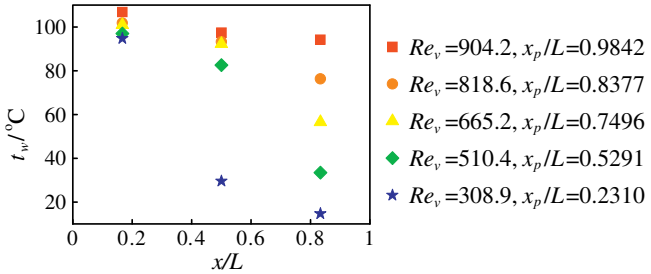

Fig. 14. Distribution of wall temperature. (The same condition with Fig. 6.)

$$\Delta p_{expansion} = \frac{\beta(1-\beta)\psi_S}{\rho_l}\left(\frac{m_c}{nA_c}\right)^2 \tag{16}$$

where β is the area ratio of the test section to the header, ψ_H and ψ_S are the homogeneous flow multiplier and the separated flow multiplier, respectively, and C_c is a coefficient of contraction.

Since the dominate force and the flow type of condensation in microchannels is different from that in conventional tubes, the predicted value by the conventional correlation is much larger than the experimental data. This comparison confirms again that the conventional pressure drop correlations for macrochannels cannot predict the two-phase pressure drop in microchannels [8,14].

Figs. 16 and 17 are the plots of the average condensation heat transfer coefficient h and the average Nusselt number Nu versus the inlet vapor Reynolds number Re_v in the wide rectangular microchannels, respectively. For a larger inlet vapor Reynolds number, the injection location is postponed, and the droplet-annular compound flow regime is extended, while the vapor slug-bubbly flow regime, whose heat transfer coefficient is much smaller than that before the injection flow, is shortened. Therefore, the average condensation heat transfer coefficient and the average Nusselt number for a whole channel are becoming larger with increasing inlet vapor Reynolds number.

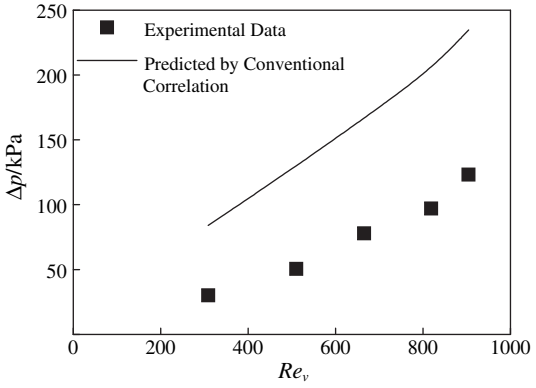

Fig. 15. Condensation pressure drop versus inlet Reynolds number. (The same condition with Fig. 6.)

Based on the experimental data, the correlation of the average Nusselt number and the inlet vapor Reynolds number in wide rectangular microchannel is expressed as

$$Nu = 9.011 \times 10^{-3} Re_v^{0.7331} \quad (17)$$

The locations of the injection flow predicted by Eq. (17) are compared with the experimental data in Fig. 18 and Table 2. The correlation coefficient and the maximum deviation of Eq. (17) from the experimental data are 0.9822 and 7.40%, respectively.

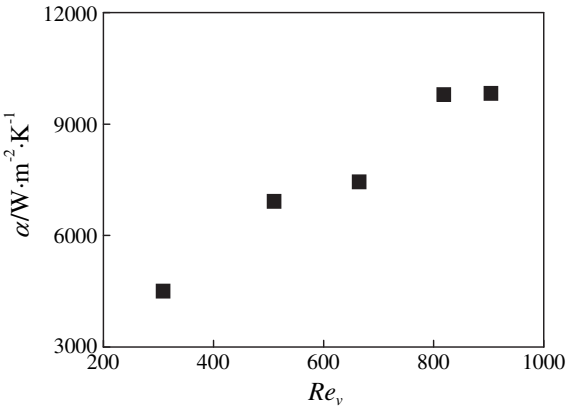

Fig. 16. Average heat transfer coefficient versus inlet vapor Reynolds number. (The same condition with Fig. 6.)

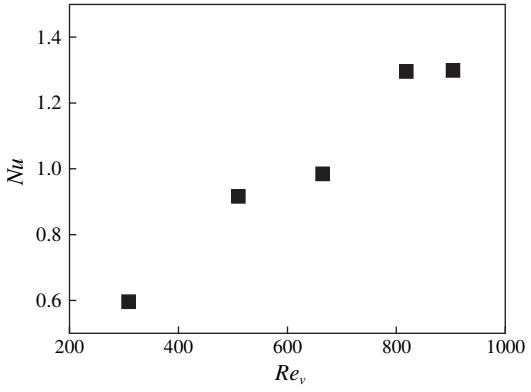

Fig. 17. Average Nusselt number versus inlet vapor Reynolds number. (The same condition with Fig. 6.)

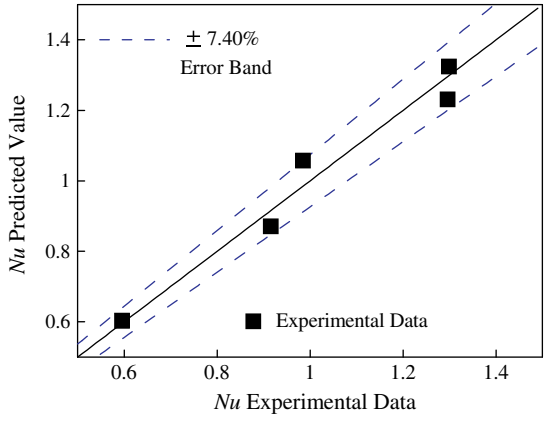

Fig. 18. Comparison between the predicted and experimental values of Nusselt number. (The same condition with Fig. 6.)

4. Conclusions

A visualization investigation on the flow condensation has been carried out in wide rectangular silicon microchannels with the width/depth ratio of 9.668 and hydraulic diameter of 90.6 μm. Based on the experimental data, the formulas of injection location, injection frequency, and the condensation Nusselt number in this wide rectangular microchannel are presented.

The main results are:

(1) Differing from the flow patterns in trapezoidal, triangular microchannels and rectangular narrows with very large width/depth ratio, the droplet-annular compound flow, injection flow, and the vapor slug-bubbly flow are observed in the wide rectangular microchannels.

(2) Droplet-annular compound flow is the dominant flow pattern at the up steam of the condensation flow. With this pattern, the short sidewalls are completely covered by the condensate due to the surface tension; however, the droplet flow still exists on the long sidewall of the channel.

(3) Injection flow is the characteristic flow pattern in rectangular microchannels. Two modes of vapor slug breakup, with a short or long vapor ligament, occur in the current microchannel. The location and the frequency of the injection flow keep stable under certain experimental conditions. With the increased inlet vapor Reynolds number, the injection location will move towards the outlet. Also, the injection frequency will increase with the increasing inlet vapor Reynolds number and condensate Weber number. The comparison between the rectangular microchannel and the triangular microchannel verifies the influence of the cross-sectional shape on the flow condensation in microchannels.

(4) The vapor slug-bubbly flow occurs after the injection flow. The vapor slug-bubbly flow can be divided into vapor slug flow and the bubbly flow. Along the condensation stream, the vapor slug will be contracted to form a round shape dominated by the surface tension. The collision and combination of bubbles may occur, and the spherical bubble without this combination will gradually condense, shrink and submerge in the condensate.

Acknowledgements

The authors gratefully acknowledge the support provided by National Natural Science Foundation of China (No.50806012).

References

[1] Y.P. Chen, M.H. Shi, P. Cheng, G.P. Peterson, Condensation in microchannels. Nanoscale Microscale Thermophys. Eng. 12 (2) (2008) 117–143.
[2] X.Z. Du, T.S. Zhao, Analysis of film condensation heat transfer inside a vertical micro tube with consideration of the meniscus draining effect. Int. J. Heat Mass Transf. 46 (24) (2003) 4669–4679.
[3] B. Médéric, M. Miscevic, V. Platel, Experimental study of flow characteristics during condensation in narrow channels: the influence of the diameter channel on structure patterns. Superlattices Microstruct. 35 (3–6) (2004) 573–586.
[4] K. Ichikawa, K. Hosokawa, R. Maeda, Interface motion of capillary-driven flow in rectangular microchannel. J. Colloid Interface Sci. 280 (1) (2004) 155–164.
[5] S. Garimella, Condensation flow mechanisms in microchannels: basis for pressure drop and heat transfer models, in: Proceedings of the 1st International Conference on Microchannels and Minichannels, Rochester, New York, 2003, pp. 181–192.
[6] S. Garimella, T.M. Bandhauer, Measurement of Condensation Heat Transfer Coefficients in Microchannel Tubes. ASME, Heat Transfer Division, Fluid-Physics and Heat Transfer for Macro-and Micro-scale Gas-Liquid and Phase-Change Flows, New York, 2001, 243–249.
[7] S. Garimella, J.D. Killion, J.W. Coleman, An experimentally validated model for two-phase pressure drop in the intermittent flow regime for circular microchannels. J. Fluids Eng. Trans. ASME 124 (1) (2002) 205–214.

[8] S. Garimella, J.D. Killion, J.W. Coleman, An experimentally validated model for two-phase pressure drop in the intermittent flow regime for noncircular microchannels. J. Fluids Eng. Trans. ASME 125 (5) (2003) 887–894.
[9] Y.P. Chen, P. Cheng, Condensation of steam in silicon microchannels. Int. Commun. Heat Mass Transf. 32 (1–2) (2005) 175–183.
[10] Y.P. Chen, J. Li, G.P. Peterson, Influence of hydraulic diameter on flow condensation in silicon microchannels, in: Proceedings of the 13th International Heat Transfer Conference, Sydney, Australia, 2006.
[11] H.Y. Wu, P. Cheng, Condensation flow patterns in silicon microchannels. Int. J. Heat Mass Transf. 48 (11) (2005) 2186–2197.
[12] H.Y. Wu, M.M. Yu, P. Cheng, X.Y. Wu, Injection flow during steam condensation in silicon microchannels. J. Micromech. Microeng. 17 (8) (2007) 1618–1627.
[13] X.J. Quan, P. Cheng, H.Y. Wu, Transition from annular flow to plug/slug flow in condensation of steam in microchannels. Int. J. Heat Mass Transf. 51 (3–4) (2008) 707–716.
[14] X.J. Quan, P. Cheng, H.Y. Wu, An experimental investigation on pressure drop of steam condensing in silicon microchannels. Int. J. Heat Mass Transf. 51 (21–22) (2008) 5454–5458.
[15] W. Zhang, J.L. Xu, J.R. Thome, Periodic bubble emission and appearance of an ordered bubble sequence (train) during condensation in a single microchannel. Int. J. Heat Mass Transf. 51 (13–14) (2008) 3420–3433.
[16] W. Zhang, J.L. Xu, Flow pattern and multichannel effect of steam condensation in silicon microchannels. J. Eng. Thermophys. 29 (4) (2008) 605–608.
[17] Y.P. Chen, R. Wu, M.H. Shi, J.F. Wu, G.P. Peterson, Visualization study of steam condensation in triangular microchannels. Int. J. Heat Mass Transf. 52 (21–22) (2009) 5122–5129.
[18] T.S. Zhao, Q. Liao, Theoretical analysis of film condensation heat transfer inside vertical mini triangular channels. Int. J. Heat Mass Transf. 45 (13) (2002) 2829–2842.
[19] H.S. Wang, J.W. Rose, H. Honda, A theoretical model of film condensation in square section horizontal microchannels. Chem. Eng. Res. Des. 82 (4) (2004) 430–434.
[20] H.S. Wang, J.W. Rose, A theory of film condensation in horizontal noncircular section microchannels. J. Heat Transf. Trans. ASME 127 (10) (2005) 1096–1105.
[21] H.S. Wang, J.W. Rose, Film condensation in horizontal microchannels: effect of channel shape, in: Proceedings of the 3rd International Conference on Microchannels and Minichannels, Toronto, Ontario, Canada, 2005, pp. 729–735.
[22] Y.P. Chen, J.F. Wu, M.H. Shi, G.P. Peterson, Numerical simulation for steady annular condensation flow in triangular microchannels. Int. Commun. Heat Mass Transf. 35 (7) (2008) 805–809.
[23] J.F. Wu, Y.P. Chen, M.H. Shi, P.P. Fu, G.P. Peterson, Three dimensional numerical simulation for annular condensation in rectangular microchannels. Nanoscale Microscale Thermophys. Eng. 13 (1) (2009) 1–17.
[24] Y.P. Chen, X. Li, M.H. Shi, J.F. Wu, One dimensional numerical simulation for steady annular condensation flow in rectangular microchannels. Heat Mass Transf. 46 (1) (2009) 75–82.
[25] E. Cormac, D. Tara, D. Mark, O. Cian, S. Orla, Direct comparison between five different microchannels, part 1: channel manufacture and measurement. Heat Transf. Eng. 26 (3) (2005) 79–88.
[26] P. Corimnne, B. Jumana, S. Christian, C. Martin, Analytic modeling, optimization, and realization of cooling devices in silicon technology. IEEE Trans. Compon. Packag. Technol. 23 (4) (2000) 665–672.
[27] U.T. Giang, D. Lee, M.R. King, L.A. Delouise, Microfabrication of cavities in polydimethylsiloxane using DRIE silicon molds. Lab. Chip 7 (12) (2007) 1660–1662.
[28] M. Callies, Y. Chen, F. Marty, A. Pépin, D. Quéré, Microfabricated textured surfaces for super-hydrophobicity investigations. Microelectron. Eng. 78-79 (1–4) (2005) 100–105.
[29] H. Teng, P. Cheng, T.S. Zhao, Instability of condensate film and capillary blocking in small-diameter-thermosyphon condensers. Int. J. Heat Mass Transf. 42 (16) (1999) 3071–3083.
[30] R.W. Lockhart, R.C. Martinelli, Proposed correlation of data for isothermal two-phase, two-component flow in pipes. Chem. Eng. Prog. 45 (1) (1949) 39–48.